Device for multifocal delivery of ultrasound into deep brain regions in humans

Thomas Riis, Daniel Feldman, Adam Losser, Brian Mickey, and Jan Kubanek, *Member, IEEE*

***Abstract*— Low-intensity focused ultrasound provides the means to noninvasively stimulate or release drugs in specified deep brain targets. However, successful clinical translations require hardware that maximizes acoustic transmission through the skull, enables flexible electronic steering, and provides accurate and reproducible targeting while minimizing the use of MRI. We have developed a device that addresses these practical requirements. The device delivers ultrasound through the temporal and parietal skull windows, which minimize the attenuation and distortions of the ultrasound by the skull. The device consists of 252 independently controlled elements, which provides the ability to modulate multiple deep brain targets at a high spatiotemporal resolution, without the need to move the device or the subject. And finally, the device uses a mechanical registration method that enables accurate deep brain targeting both inside and outside of the MRI. Using this method, a single MRI scan is necessary for accurate targeting; repeated subsequent treatments can be performed reproducibly in an MRI-free manner. We validated these functions by transiently modulating specific deep brain regions in two patients with treatment-resistant depression.**

***Index Terms*— ultrasound, neuromodulation, focused, beamforming**

I. Introduction

Transcranial focused ultrasound provides a new set of approaches to noninvasively manipulate neural activity in spatially circumscribed deep brain targets [1], [2]. The approaches have included transient [3], [4] and durable [5]–[7] modulation of neural circuits, and the delivery of specific drugs across the intact [8], [9] and transiently opened [10] blood-brain barrier. Unlike other noninvasive approaches, ultrasound-based approaches reach millimeter-level precision deep in the brain [11]. However, clinical translation has been impeded by challenges associated with ultrasound distortions by the skull, lack of flexible targeting, and the complexity and cost of transducer to subject registration. These issues reduce the control over the delivery of ultrasound to brain areas of interest, thus limiting the safety and effectiveness of therapeutic applications.

The human skull poses a formidable barrier for ultrasound [12], [13]. For example, the intensity of neuromodulatory ultrasound is attenuated by human skull alone by a factor of 4.5–64, depending on skull segment and individual [14]. Previous studies [14]–[16] found that delivery of the ultrasound through the temporal and parietal bone minimizes the severity of the aberrations, both in terms of the ultrasound dephasing and its attenuation. We designed a device that focuses ultrasound through these areas to minimize the impact of the skull distortions.

Mental and neurological disorders involve distributed neural networks [17]–[22]. The distributed nature of these representations requires the ability to flexibly steer the ultrasound target throughout the brain. Phased array technology has been used to implement this feature [23]. We designed our device using two phased arrays with the goal of maximizing the volume in which the ultrasound can be refocused. This approach enables operators to precisely address multiple targets through a large volume of the brain rapidly without the need for moving the subject or the device.

And finally, repeated therapeutic applications require accurate registration to patient-specific anatomy. This can be achieved using MRI guidance [24]–[26]. However, most current applications of reversible, low-intensity ultrasound require repeated applications. For such applications, positioning subjects in MRI repeatedly would incur high cost and thus impede treatment reimbursement. To address this issue, we have developed an approach that uses noninvasive mechanical registration for accurate targeting of deep brain areas both inside and outside of the MRI scanner. The registration requires a single MRI scan of the subject's head.

We validated these key functions by deploying the device in two patients with major depression. The stimulation modulated mood states and was well tolerated with no adverse events.

II. Materials and Methods

A. Ultrasonic Device

1) Arrays: The device consists of two spherical phased array transducers mounted to a plastic, MRI compatible frame such that they are positioned opposite to each other and separated by a distance of 187 mm (**Fig. 1**). These transducers delivered ultrasound through the parietal and temporal bones of a subject. Specifically, the transducers were positioned parallel to the left and right sides of a subject's head.

The array elements are made of PMN-PT material, with a square surface geometry of 6 mm x 6 mm, and operate at a fundamental frequency of 650 kHz. The rated acoustic power at the transducer surface was 3 W/cm^2 (**Suppl. Fig. 2**). The two spherically focused arrays have a radius of 165 mm, 126 elements in a 9 x 14 element grid, with inter-element spacing

T. R., A. L., B. M., and J. K. are with the Department of Biomedical Engineering, University of Utah, UT 84112 USA (corresponding e-mail: tom.riis@utah.edu).

D. F. and B. M. are with the Department of Psychiatry, Huntsman Mental Health Institute, University of Utah, UT 84112 USA.

of 0.5 mm. Each array has a height of 55 mm and a width of 86 mm, spanning an area of 47.3 cm^2. The array elements are housed in rectangular plastic casing with height of 65.83 mm, width of 98.8 mm, and depth of 66.43 mm. Each element is connected to an insulated copper wire (38 AWG) that terminates in an impedance-matching network matched at the transducers' 650 kHz driving frequency. (Doppler Electronic Technologies).

Both transducers were driven by a programmable driving electronics system with 256 output channels (Vantage256, Verasonics). The driving system additionally used a high-voltage dual 600 W DC power supply (QPX600DP, Aim and Thurlby Thandar Instruments). The tranducers were connected to the Verasonics using DL5-260P connectors which terminated in an impedance-matching network. The transducers and matching network are connected by a 9-meter-long cable that is detachable from the matching network such that it can be passed through MRI waveguides.

2) Coupling: Coupling was mediated using a hydrogel [27]. Standard ultrasound coupling gel was applied to the interfaces between the transducer and the hydrogel, and the hydrogel and the head.

3) Registration: We mechanically registered the device to the subject's brain anatomy. In particular, we immobilized the subject's head using a standard thermoplastic mask (Aquaplast U-Frame, QFix). Lateral windows are made within the mask, exposing the left and right sides of the subject's head, for unobstructed ultrasound propagation. Once the head was fixed using the mask, we took a single T1 MRI with the arrays mounted on the subject over the brain target of interest. The MRI field of view included both the subject's brain anatomy and the arrays with fiducial markers. Using the fiducial markers, we then registered the transducer geometry within the MRI image of the patient's brain. The plastic frame that holds the arrays slides on horizontal and vertical tracks and can be locked in specific discrete positions. This allows the arrays to be placed repeatedly over any section of the left and right sides of the head for targeting of nearly the entire deep-brain volume. In subsequent sessions outside the MRI, we manually locked the arrays in the same position as during the MRI session and applied the same thermoplastic mask to position the subject's head in the same location with respect to the arrays. This step reproduces the position of the arrays and the subject's head in the same configuration imaged inside the MRI. Thus we then used the anatomical MRI data of this configuration with the registered transducers in all subsequent sessions outside the MRI for subject-specific targeting.

4) Targeting: Beamforming with ultrasound phased arrays consists of emitting ultrasound from each element with delays such that the wavefronts arrive into the defined target at the same time, so that they constructively interfere. These delay values can be calculated by knowing the distance from each element to the target and dividing by the speed of sound over the acoustic path. The distance from each element to the brain target is known from the MRI image of the transducer mounted on the subject, where both the transducers and the subject's brain are in the same image space. We use the speed of sound in water to set the initial delays to focus at target and add the estimated phase shifts from any skull correction method to account for phase shifts induced by coupling, hair, scalp, skull, and brain. We then apply these delays, the sum of the focusing in water and the estimated phase shifts to focus into the target in the brain.

5) Relative Through Transmit Skull Correction: With the dual array setup, we employed through-transmit measurements to assess how the skull is distorting the incoming beams of ultrasound and compensate for these aberrations. Specifically, we applied the correction algorithm as follows:

1) The transducers emitted a 10-cycle, 650 kHz pulse individually from each of its 126 elements while recording responses from all the other, non-transmitting elements on the opposing transducer. During the through-transmit scans, the peak pressure amplitude of each transducer element is 80 kPa (**Suppl. Fig. 2**). The entire process of this scan takes less than one second to complete. The 650 kHz pulse frequency is the same as that used for the neuromodulation. This through-transmit measurement is relativistic: it is performed with the subject present and absent. When the subject is absent, the measurement is made through water. It requires no prior information about the subject's anatomy or CT/MRI images of the head. Let $s_{ij}(t)$ represent this signal received on a transducer i after a brief, 10-cycle pulse is emitted from a transducer j. Let the signals received in free field and through the acoustic barriers (skull, hair, coupling, and other barriers) be denoted as $s_{ij}^F(t)$ and $s_{ij}^B(t)$, respectively.
2) The method compares the through-transmit measurements in water, $s_{ij}^F(t)$, with those taken through the subject, $s_{ij}^B(t)$, to estimate the phase shift, τ_i, and amplitude, A_i, distortions introduced by the subject's head for each element i. The through-transmit attenation from element j to element i, A_{ij}, is measured by dividing the peak amplitudes of the through-transmit waveforms through the subject versus through water, when there is no barrier to transmission:

$$A_{ij} = \frac{max(s_{ij}^B(t))}{max(s_{ij}^F(t))} \tag{1}$$

The attenuation through the two opposite sides of the skull are multiplicative, hence $A_{ij} = A_i A_j$, where A_i is the attenuation factor for element i, and the value we must estimate in order to compensate for the skull and other barriers in front of this element. To estimate this value for element i, we first selected through-transmit pairs where the angle between the transmitting transducer i and the target and the transmitting transducer i and the receiving transducers was less than or equal to 7°. A_i is then estimated as the square root of the median through-transmit value between i and the selected receive elements. Phase correction is estimated similarly by finding the phase shifts τ_{ij} that minimize the cross correlation between the waveforms $s_{ij}^F(t)$ and $s_{ij}^B(t)$. Previous work discusses the details of this method [28].

3) Once the phase and amplitude values are estimated, we automatically adjust the stimulation parameters to compensate for the distortions. With the attenuation values A_i estimated for each element, we scale the voltage applied to element i by $1/A_i$ in order to compensate for this attenuation. If A_i is less than a threshold value of 0.1, the element is turned off to avoid overdriving the element. Similarly, with the speed up through the skull estimated as τ_i, we delay the emission time of this element by the same value so that the waveforms compensate for this distortion.

In the stimulation sessions, the correction was performed online and took approximately 2 minutes to complete.

B. Human Subjects

The hardware and stimulation described in this article were considered non-significant risk by the Institutional Review Board of University of Utah and approved to be applied in patients with major depression (NCT05301036). Subjects included in this study have a primary diagnosis of major depressive disorder or bipolar disorder and a self-rated 16-item Quick Inventory of Depressive Symptomatology (QIDS) total score greater than 10. All subjects provided informed consent. Two patients (female, aged 32 and 35) with history of severe treatment-resistant depression were recruited in the study.

C. Neuromodulation Parameters

The effects on mood reported in this study were measured at the Huntsman Mental Health Institute, in a sonication session outside of the MRI. The ultrasound was delivered into each target in 30 ms ON periods (650 kHz, 1.0 MPa peak pressure, estimated using the relative through transmit skull correction method [28]), $MI = 1.2$, $I_{SPPA} = 31$ W/cm^2) followed by 4 s OFF periods (0.75% duty, $I_{SPTA} = 0.233$ W/cm^2). Sonication duration varied from 60-180 s.

1) Active Sham: We controlled for the potential artifacts that can be associated with the application of ultrasound through the head. Specifically, we developed an active sham condition that used the same waveform and emission voltages but was not focused into a specific target. The ultrasound emission times were set such that each transducer emitted an unfocused, planar wave from the face of the transducer in the axial dimension (**Suppl. Fig. 3**). The power applied to the transducer and the pressure emitted from each element was the same as during the verum stimulation. This way, the subjects' head experienced equal energies and waveforms in both the verum and the active sham conditions, yet the spatial peak pressure inside the brain for the plane wave (0.098 MPa, 0.30 W/cm^2) were an order of magnitude lower than the focused condition (1 MPa, 31.1 W/cm^2) (**Suppl. Fig. 3**).

D. Evaluation of Effects on Mood and Side Effects

We used a 7-point scale to measure changes in subject mood states: Depression and Anxiety. For example, the scale for depression ranged from -3, "much less depressed", to 3, "much more depressed", with 0 indicating no change. A psychiatrist asked the subject to rate their mood immediately following each sonication. Additionally, the subject filled out the Generic Assessment of Side Effects (GASE) questionnaire prior to enrolling in the trial and at the end of each sonication session. The subject was asked to rate each of 36 different symptoms from 0-not present, 1-mild, 2-moderate, 3 severe, and note if they found this symptom related to the treatment.

E. Study Protocol

The first visit took place inside an MRI suite (Magnetom VIDA, 3T, Siemens). Prior to the imaging, we molded the thermoplastic mask on the patient's face, coupled the device to the patient's head, and took structural MRI images for the previously described registration. The second, MRI-free visit was performed at the Huntsman Mental Health Institute. The subject's head was immobilized in the same thermoplastic mask and the arrays locked in the same position as during the initial visit. We delivered ultrasonic stimulation into the subgenual cingulate cortex and the ventral striatum. The targets were presented randomly, in a blinded manner, and were interleaved with the above described active sham stimulation (plane waves) over a 1.5 hour neuromodulation session.

F. MRI

We collected all imaging data with a 3T MRI scanner (Magnetom Vida, Siemens) at the Imaging Neuroscience Center at the University of Utah. We placed a Siemens flex coil (size: small) over the anterior and superior aspects of the subject's head to maximize the signal-to-noise ratio of the acquired signals.

1) Anatomical Acquisition: T1 anatomical images were collected using a magnetization prepared radio frequency pulses and rapid gradient echo (MPRAGE) sequence with an ascending, anterior to posterior acquisition of 192 sagittal slices with thickness of 1.3 mm. The repetition time (TR) was 2400 ms, echo time (TE) was 2.26 ms, inversion time (TI) was 1060 ms, and echo spacing was 6.84 ms. The field of view (FOV) was 256 mm, with bandwidth of 200 Hz/pixel and a flip angle of 8 degrees.

G. Measurements of steering range and focal volume

1) Skulls: Four intact *ex-vivo* human skulls were used in this study. The skulls were obtained from Skulls Unlimited (Oklahoma City, OK). The supplier provides *ex-vivo* specimens specifically for research under a research agreement. A large opening was made at the bottom of each skull to enable field measurements inside the skull (**Suppl. Fig. 1**). Each skull was degassed overnight in deionized water [12]. Following the degassing at -25 mmHg, the skull was transferred, within the degassed water, into an experimental tank filled with continuously degassed water (AIMS III system with AQUAS-10 Water Conditioner, Onda).

2) Steering range: Beamforming range was measured inside four ex-vivo skulls with hydrophone field scans. At each location in the scans, elements were fired individually, and the received signals recorded. The total pressure at each point was taken as the sum of these individual waveforms under perfect focusing through the skull. Perfect focusing entails adjusting the delays on the received signals from each element such that they arrive at the hydrophone at the same time, perfectly in phase. Delays are found by maximizing the cross-correlation between all waveforms. The scans were performed over 2D planes in the XY, XZ, and YZ planes with the span of the X (axial), Y (lateral), and Z (elevational) dimensions being 80 mm, 60 mm, 56 mm respectively, all with 1.5 mm step size. These 2D scans were then interpolated to a resolution of 0.2 mm and the full width half max (FWHM) distance in each dimension was calculated about the origin defined as the geometric center of the two arrays. In the X dimension, the FWHM value exceeded the scan bounds that were constrained to $\pm$ 40 mm by the width of the ex-vivo skulls. To estimate the entire FWHM in this dimension, we fit a 2nd-degree polynomial to the measured field in the X dimension about the origin and extrapolated the field profile out to $\pm$ 100 mm. The FWHM was calculated as the difference in the X coordinates where the extrapolated field profile first fell below 50% of the peak value.

3) Pressure Field Hydrophone Scans: A capsule hydrophone (HGL-0200, Onda) secured to 3-degree-of-freedom programmable translation system (Aims III, Onda) was used to record the ultrasound field emitted from each element. The hydrophone has a sensitivity of -266 dB relative to 1 V/μPa and aperture size of 200 μm. This aperture size is well within the ultrasound wavelength (2.3 mm). The 3D field measurements use a step size of 0.2 mm to provide high spatial resolution of each element's contribution to the total field. The hydrophone scans measured 40 x 40 mm planar scans in all three dimensions (XY, XZ, and YZ).

The scans were performed at the geometric center of the two arrays in water and through an *ex-vivo* human skull. At each location in the scans, elements were fired individually, and the received signals recorded. Since ultrasound pressure is additive, the total pressure was computed as the sum of the individual constituents.

4) Focal volume: We quantified the focal volume of the arrays by measuring the total size of the intensity field above half the maximum value. Specifically, we took the convex hull of the voxels just exceeding the half-maximum intensity in both the XY and XZ planes. For each position on the x-axis, we calculated the full width half max—the width of the focal volume at half-maximum intensity—in the Y and Z dimension. We then integrated these products over the x axis to get the total volume. In particular, let the functions $FWHM_y(x)$ and $FWHM_z(x)$ denote the full width half max at position x in the Y and Z dimension, respectively. The focal volume then equals $\int FWHM_y(x)FWHM_z(x)dx$.

H. Measurements of positioning reproducibility

We quantified the session-to-session registration error across 5 human subjects by measuring the position variability of both the device and the subject. In particular, we used an optically tracked stylus (Brainsight, Rogue Resolutions Ltd.) to record the position of six fiducial markers on the transducer arrays and four anatomical landmarks on the subject (tip of the nose, left and right corners of the eye, and a mark on the left temple). We performed this measurement across 10 trials per subject. Before each session, we re-instantiated the device and the subject to simulate a new treatment session. After each session, the subject was taken out of the thermoplastic mask and asked to stand up and walk away from the table. The device was unscrewed from its locked position and reset to its reference position. Each fiducial and anatomical landmark was measured three times with the stylus. The median of these three measurements was used as the fiducial's position.

We measured the variability in position of the device and subject by calculating the mean location of each fiducial for each subject across all trials, and subtracted that number from the fiducial positions. Next, we calculated the combined variability of the subject and the device by taking the difference of each fiducial on the device from each fiducial on the subject. We then measured the deviation from the mean in these distances for each pair across trials. The targeting accuracy constituted the average relative position variability across all fiducial pairs.

III. Results

We have developed a device for neuromodulation of specified deep brain regions in humans. The device consists of two sets of ultrasound transducer arrays positioned at opposite sides of the head (**Fig. 1a**). The dual phased arrays enables the device to electronically focus the ultrasound into specified deep brain targets and deliver ultrasound specifically through the relatively acoustically permissive areas of the skull—the parietal and temporal bone [14]–[16], [29].

Prior to an application, the subject's head is immobilized using an individually fitted, standard radiological mask (**Fig. 1b**). Lateral windows in the mask enable the ultrasound to propagate into the head using a coupling medium (Methods). The device is MRI-compatible (**Fig. 1c-d**). The MRI provides the means for accurate registration of the device with respect to the subject's brain anatomy. Since the mask is attached to the same platform as that which holds the transducers, this MRI-based registration procedure only requires one MRI scan. Subsequent applications can be reproducibly performed without an MRI, as is shown further.

Fig. 1c-d shows the intensity fields produced by the device, overlaid on a patient's brain anatomy. For the specified target of the subgenual cingulate cortex (SGC), the intensity field had lateral x elevational x axial dimensions of 2.4 mm x 3.6 mm x 20.4 mm (y, z, and x dimensions of the Montreal Neurological Institute coordinate system). The total field volume of 0.142 cm^3 was equivalent to a sphere with a radius of 3.24 mm.

The phased-array device has the ability to focus the ultrasound into specified targets electronically, without moving the subject or the device. **Fig. 2a** shows, in yellow-red colors, an example field associated with a focal point measured inside an ex-vivo human skull. The device can steer the focal point

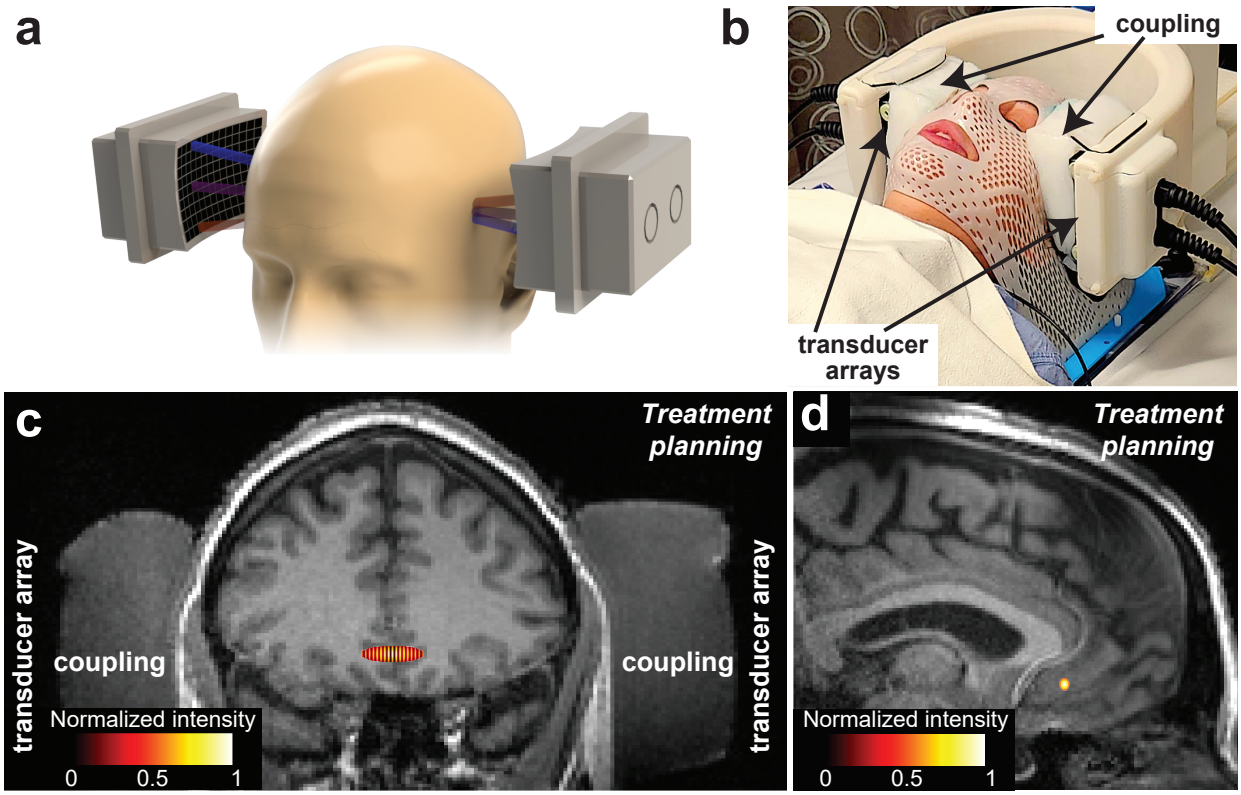

Fig. 1: **Approach and hardware for flexible delivery of ultrasound into deep brain targets.**
a, Hardware. Programmatic, electronic focusing is achieved using two sets of 126 individually controlled transducer elements, one over the left and one over the right side of the head (black). This design delivers ultrasound through the relatively permissive portions of the skull—the temporal and parietal bone [14]–[16], [29]. **b, Application.** The subject's head is secured in place using a standard radiological mask (Methods). Lateral windows are made within the mask for unobstructed ultrasound propagation. Coupling is mediated using cryogel (Methods). Ultrasonic arrays are mounted within a MRI compatible frame that positions the arrays within a specific location in the anterior-posterior and superior-inferior axes. **c-d, Treatment planning**. Coronal (c) and sagittal (d) views of subject-specific brain anatomy. Computed fields (**Suppl. Fig. 3**) are superimposed on the subject-specific anatomy to label the target for the operator (subgenual cingulate cortex, in this case).

through beamforming to modulate single or multiple targets [30] within a relatively broad treatment envelope (**Fig. 2**, blue). The addressable space within which the device delivers at least half of its maximal pressure, measured using hydrophone inside four *ex-vivo* skulls, spans 110.8 $\pm$ 5.69 mm, 46.1 $\pm$ 3.4 mm, 44.8 $\pm$ 2.7 mm (mean $\pm$ s.d.) in the axial, lateral, and elevational dimensions, respectively (**Fig. 2b**). To target additional parts of the brain, the frame that holds the transducers (**Fig. 1b**) can be physically translated in the patient's anterior-posterior and superior-inferior dimensions to target particular regions of interest.

For cases in which cost is an important factor, the device can be applied outside the MRI scanner after a single MRI session that registers the relative position of the head and the device. This mode of operation is possible by immobilizing a subject's head with a standard radiological mask (**Fig. 1b**). Moreover, the plastic frame provides reproducible positioning of the ultrasound transducers. We evaluated the registration error between the head and the transducers in five subjects across ten sessions. Across all sessions ($n = 10$ in each subject), the ultrasound transducers' position was displaced from their initial position on average by 0.89$\pm$0.64 mm (mean$\pm$s.d.). Within each dimension (x, y, z), the transducers were displaced by 0.45$\pm$0.32 mm, 0.43$\pm$0.14 mm, and 0.44$\pm$0.17. The error in the head positioning was also within the acceptable range. Using fiducial markers positioned on the subjects' head, we detected an average error of 1.28$\pm$0.66 mm, and 0.53$\pm$0.19 mm, 0.68$\pm$0.27 mm, and 0.71$\pm$0.31 mm in the x, y, and z dimensions across all subjects and sessions. We then computed the relative error between the transducer and the subject's head, which is the ultimate metric that informs on the targeting accuracy. The relative error was 1.64$\pm$0.66 mm across subjects and 0.77$\pm$0.50 mm, 0.93$\pm$0.41 mm, and 0.99$\pm$0.49 in the x, y, and z dimensions (**Fig. 3**).

We deployed the device to modulate the SGC in two patients with treatment-resistant depression (NCT05301036). Major depression is commonly associated with hyperactive SGC [31]. We therefore hypothesized that a transient suppression of the SGC should improve subjective mood states. To suppress neural activity, we delivered the ultrasound into the target at a low duty cycle value, which tends to inhibit neuronal activity [32]–[34]. Indeed, the modulation of the SGC had a positive effect on metrics of depression and anxiety in both subjects (**Fig. 4**). Stimulation of the SGC for duration 60 seconds and longer led to significant improvements in depression (t_{18}=3.54, p=0.0012, two-tailed t-test) and anxiety (t_{18}=2.87, p=0.0051,

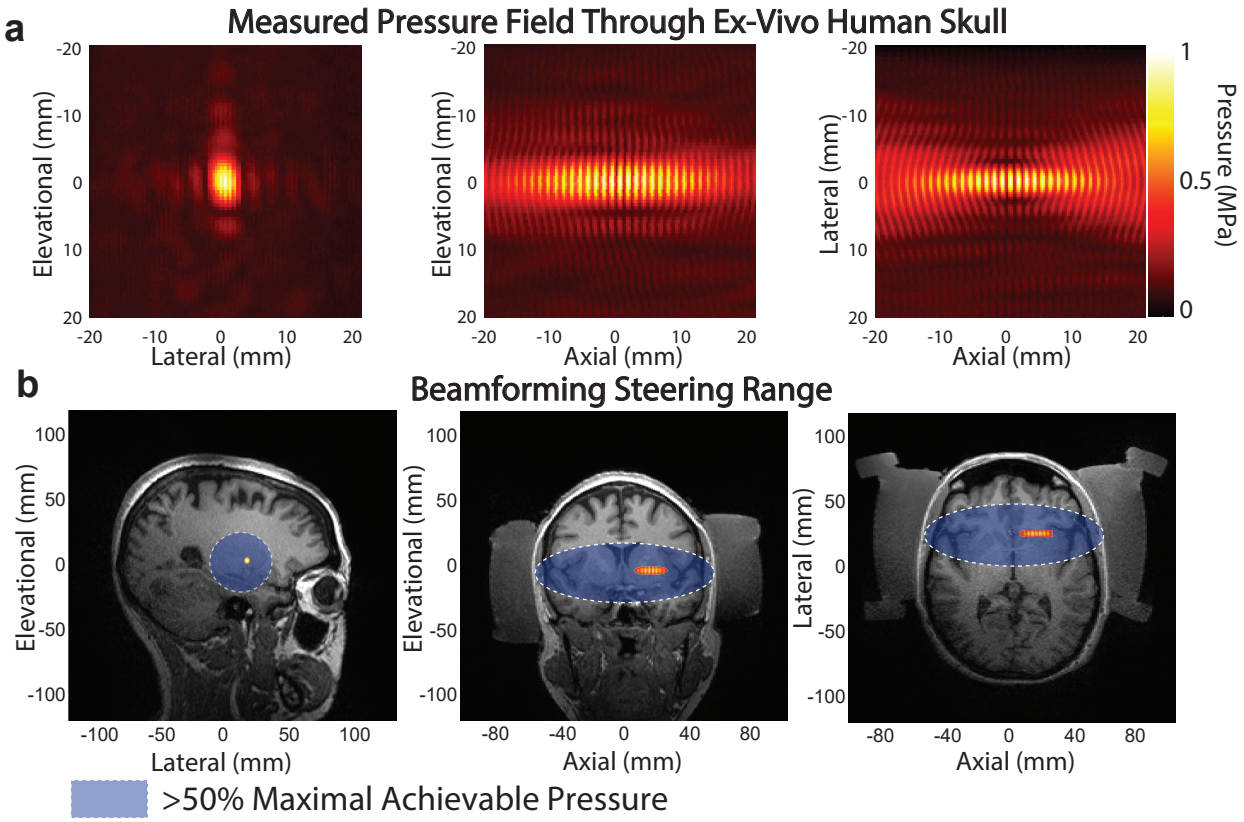

Fig. 2: **Deep brain focusing and steering.**
a, Example pressure field measured in three dimensions through an ex-vivo human skull. The middle and right panels show that the two arrays produce a notable standing wave, as expected. **b,** Electronic targeting range (blue) measured through four ex-vivo skulls. The white boundaries outline the regions in which the device can deliver 50% of its maximal pressure output. The fields were measured inside an ex-vivo human skull and overlaid on anatomical MRI for comparison. Any target within this region can be reached within a few dozens of microseconds [30].

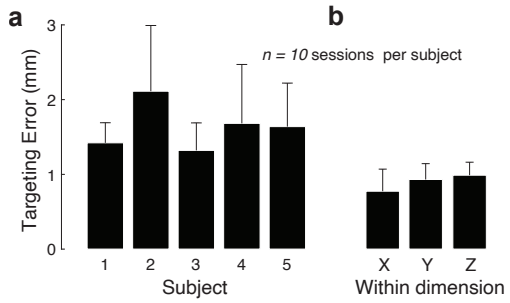

Fig. 3: **Targeting reproducibility for MRI-free operation.**
a, Mean±s.d. difference between the relative distance of the transducers and markers placed on the head. The measurements were performed in 5 subjects, $n = 10$ sessions each. **b,** The difference separately for each dimension averaged over all subjects.

two-tailed t-test) metrics. Sham stimulation caused no significant effects on depression (t_7=1.53, p=0.17) or anxiety (t_7=0, p=1).

We evaluated the safety of the stimulation at the behavioral and anatomical levels. At the behavioral level, subjects completed a standard clinical side effect questionnaire [35]. No adverse effects were noted by either subject or the attending psychiatrist. At the anatomical level, we collected structural T1-w and T2-w MRIs of the brain. No apparent changes were evident.

IV. Discussion

We have developed an approach and hardware that 1) minimizes the distortions that ultrasound experiences when propagating through the skull 2) provides flexible electronic targeting of deep brain regions 3) uses mechanical registration for practical, low-cost registration inside and outside of an MRI. We used this device to stimulate deep brain targets in two patients with major depression and observed target-specific improvements in mood states.

The propagation through the temporal-parietal windows maximizes the ultrasound transmission into the head. However, this feature should be complemented by approaches that can accurately correct for all aberrations of ultrasound by the skull. On this front, the device is designed to accommodate many of the existing and emerging approaches for skull correction [11], [28], [29], [36]–[40]. All elements of the phased arrays are controlled independently. This way, it is possible to adjust the emission time and amplitude separately for each element, thus achieving the sought correction optimum with respect to the method of choice.

The phased arrays provide the capacity to target many regions within the deep brain (**Fig. 2**). For instance, the modulation of the SGC in subject A required to steer the focus

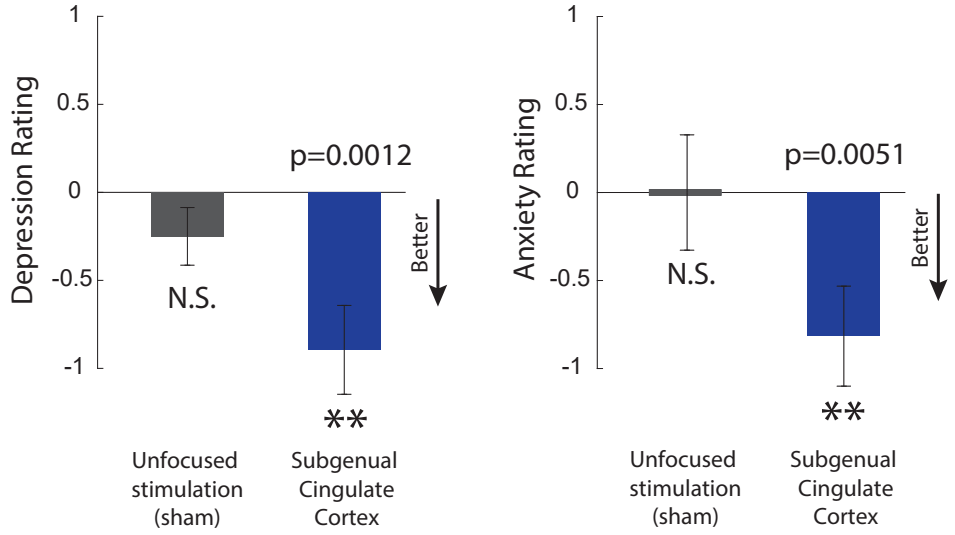

Fig. 4: **Noninvasive deep brain stimulation is capable of improving mood states in patients with major depression.** Combined self-reported mood scores across patients following each stimulation (27 stimuli; **Suppl. Fig. 4**). A psychiatrist assessed changes in the subjects' mood immediately following each stimulus, measuring changes to depression on a seven-point scale from -3 (indicating much less depressed) to 3 (much more depressed) with 0 representing no change. Sham stimulation delivered into the brain had the same energy and waveform but was not focused. This controls for potential generic auditory and tactile artifacts that could be associated with transcranial ultrasound. Subjects were blinded to the individual stimuli. There were positive effects on mood following the modulation of the SGC for at least 60 s, but not in other cases including sham stimulation.

17 mm laterally and 9 mm elevationally from the geometric center of the arrays. The electronic beamforming also enabled ultrasound delivery into the superior and inferior sections of the subgenual cingulate cortex, as well as the ventral striatum (**Suppl. Fig. 4**). The capacity to electronically deliver ultrasound into different targets in less than a millisecond could lead to the development of rapid stimulation sequences that modulate neural networks in precise spatiotemporal patterns. This capacity is expected to prove crucial for effective treatments of mental and neurological disorders, which require high targeting precision as well as flexibility in targeting distant nodes of neural networks [31], [41]–[46].

The device and data acquisition approach are designed to minimize the need for MRI, with the goal of reducing treatment cost. A single MRI image provides sufficient information for registration. Subsequent therapeutic sessions can be performed in an MRI-free manner (**Suppl. Fig. 4**). This is achieved by immobilizing the patient's head in a fixed location with respect to the transducers, and reproducing this positioning outside of MRI during subsequent stimulation sessions. We found that the re-positioning of the subject's head and transducers is reproducible from session to session, with a relative positioning error between fiducial markers on the subject and the transducers of 1.64 mm on average (**Fig. 3**). The mechanical registration method allows for accurate targeting of deep brain areas inside and outside of an MRI scanner. The operation in the MRI opens a path to new tools for validating and monitoring the ultrasound delivery [24], [47]–[49]. For MRI-free operations, the thermoplastic mask provides a convenient approach to mitigate the costs associated with optical neuronavigation systems [48], [50], [51].

The device can be used for two main applications—diagnostic and therapeutic. The ability to flexibly modulate specified deep brain targets (**Suppl. Fig. 4**) will provide a unique tool to guide invasive approaches such as deep brain stimulation or ultrasonic ablative brain treatments [11]. By precisely modulating candidate targets in sequence, it is possible to determine the brain region that maximizes the sign or symptom improvement in each individual patient. This region constitutes the target for a subsequent invasive treatment. The flexible neuromodulation also provides a unique tool for manipulation of deep brain structures, which can further our causal understanding of human brain function. By systematically modulating specific brain regions, investigators will be equipped to determine how these regions are causally involved in given behaviors.

The potential for effective treatments is equally promising. When low-intensity ultrasound is applied to the brain for a sufficient amount of time (e.g., about 150 s used here; **Fig. 4**), it induces durable effects within the stimulated structures [52]–[60]. These neuroplastic effects are believed to be mediated, at least in part, by activation of glial cells and the ensuing effects on synaptic processes [6]. These effects provide a unique opportunity for durable circuit reset, akin to electroconvulsive therapy or repeated applications of TMS, but now in a much more targeted manner. The targeted nature of the stimulation is expected to increase treatment effectiveness and safety and provide a treatment option to patients for whom the current approaches are inadequate.

The device and study have several limitations. First, the axial resolution is, albeit sharper than for single-element devices [4], [61], limited (**Fig. 1c**, **Fig. 2a**). Second, it is not clear whether the average error of 1.6 mm between the subject and transducer fiducials for MRI-free operation is sufficient for accurate targeting. Dephasing of the ultrasound caused by the skull will impart additional targeting error. This issue has

a straightforward albeit costly solution—if accuracy higher than this level is required, the device can be operated inside MRI during every application. Third, the device is limited by its placement over the left and right sides of the skull. Although this positioning is favorable in terms of ultrasound transmission, it precludes access to some cortical targets at the surface of the brain. Finally, this work has focused on the design, key beneficial features, and proof-of-concept deployment of the device in a limited two patient dataset instead of on systematic investigations of the multidimensional space of ultrasound stimulation parameters and effects on mood across many patients. These investigations are expected to be accelerated though multi-institutional collaborations.

In summary, we have developed a device for noninvasive modulation of deep brain structures in humans. The system's phased arrays deliver ultrasound through parietal and temporal skull regions and offer high targeting precision and flexibility. The device enables integration with MRI for treatment guidance and monitoring and practical subsequent MRI-free operation. We demonstrated a proof-of-concept application of the device in two patients with no adverse effects. The device is expected to guide existing invasive therapies, further our causal understanding the function of deep brain circuits in humans, and accelerate the use of sustained ultrasound stimulation and ultrasound-based local drug release to provide therapeutic options for the large number of treatment-resistant patients.

Ethical Statement

This research was conducted in accordance with the principles embodied in the Declaration of Helsinki and in accordance with local statutory requirements. The hardware and stimulation described in this article was considered non-significant risk by the Institutional Review Board of University of Utah and approved to be applied in patients with major depression (Protocol #00148802) and in healthy individuals (Protocol #00127033). All subjects provided informed consent.

Acknowledgments

This work was supported by the NIH grants R00NS100986, RF1NS128569, and by grants from the Margolis Foundation, the University of Utah Vice President for Research, the Mildred P. Hunter Foundation, and University of Utah Partners for Innovation, Ventures, Outreach & Technology. The methods described herein are subject to a patent.

References

[1] A. Fomenko, C. Neudorfer, R. F. Dallapiazza, S. K. Kalia, A. M. Lozano, Low-intensity ultrasound neuromodulation: An overview of mechanisms and emerging human applications, Brain stimulation (2018).

[2] Y. Meng, S. Suppiah, K. Mithani, B. Solomon, M. L. Schwartz, N. Lipsman, Current and emerging brain applications of mr-guided focused ultrasound, Journal of therapeutic ultrasound 5 (1) (2017) 26.

[3] M. D. Menz, Ö. Oralkan, P. T. Khuri-Yakub, S. A. Baccus, Precise neural stimulation in the retina using focused ultrasound, The Journal of Neuroscience 33 (10) (2013) 4550–4560.

[4] J. Kubanek, J. Brown, P. Ye, K. B. Pauly, T. Moore, W. Newsome, Remote, brain region–specific control of choice behavior with ultrasonic waves, Science Advances 6 (21) (2020) eaaz4193.

[5] R. F. Dallapiazza, K. F. Timbie, S. Holmberg, J. Gatesman, M. B. Lopes, R. J. Price, G. W. Miller, W. J. Elias, Noninvasive neuromodulation and thalamic mapping with low-intensity focused ultrasound, Journal of Neurosurgery (2017) 1–10.

[6] S.-J. Oh, J. M. Lee, H.-B. Kim, J. Lee, S. Han, J. Y. Bae, G.-S. Hong, W. Koh, J. Kwon, E.-S. Hwang, et al., Ultrasonic neuromodulation via astrocytic trpa1, Current Biology 29 (20) (2019) 3386–3401.

[7] K. Zeng, G. Darmani, A. Fomenko, X. Xia, S. Tran, J.-F. Nankoo, Y. Shamli Oghli, Y. Wang, A. M. Lozano, R. Chen, Induction of Human Motor Cortex Plasticity by Theta Burst Transcranial Ultrasound Stimulation, Annals of Neurology 91 (2) (2022) 238–252. doi:https://doi.org/10.1002/ana.26294.
URL https://onlinelibrary.wiley.com/doi/abs/10.1002/ana.26294

[8] J. B. Wang, M. Aryal, Q. Zhong, D. B. Vyas, R. D. Airan, Noninvasive ultrasonic drug uncaging maps whole-brain functional networks, Neuron 100 (3) (2018) 728–738.

[9] H. Lea-Banks, M. A. O'Reilly, K. Hynynen, Ultrasound-responsive droplets for therapy: A review, Journal of Controlled Release 293 (November 2018) (2019) 144–154. doi:10.1016/j.jconrel.2018.11.028.

[10] N. Lipsman, Y. Meng, A. J. Bethune, Y. Huang, B. Lam, M. Masellis, N. Herrmann, C. Heyn, I. Aubert, A. Boutet, et al., Blood–brain barrier opening in Alzheimer's disease using MR-guided focused ultrasound, Nature Communications 9 (1) (2018) 2336.

[11] P. Ghanouni, K. B. Pauly, W. J. Elias, J. Henderson, J. Sheehan, S. Monteith, M. Wintermark, Transcranial MRI-guided focused ultrasound: a review of the technologic and neurologic applications, American Journal of Roentgenology 205 (1) (2015) 150–159.

[12] F. J. Fry, J. E. Barger, Acoustical properties of the human skull, The Journal of the Acoustical Society of America 63 (5) (1978) 1576–1590.

[13] P. J. White, G. T. Clement, K. Hynynen, Longitudinal and shear mode ultrasound propagation in human skull bone, Ultrasound in medicine & biology 32 (7) (2006) 1085–1096.

[14] T. Riis, T. Webb, J. Kubanek, Acoustic properties across the human skull, Ultrasonics 119 (2022) 106591. doi:https://doi.org/10.1016/j.ultras.2021.106591.

[15] B. D. Lindsey, S. W. Smith, Pitch-catch phase aberration correction of multiple isoplanatic patches for 3-D transcranial ultrasound imaging, IEEE Transactions on Ultrasonics, Ferroelectrics, and Frequency Control 60 (3) (2013) 463–480. doi:10.1109/TUFFC.2013.2590.

[16] A. Y. Ammi, T. D. Mast, I.-H. Huang, T. A. Abruzzo, C.-C. Coussios, G. J. Shaw, C. K. Holland, Characterization of ultrasound propagation through ex-vivo human temporal bone., Ultrasound in medicine & biology 34 (10) (2008) 1578–1589. doi:10.1016/j.ultrasmedbio.2008.02.012.

[17] J. L. Price, W. C. Drevets, Neural circuits underlying the pathophysiology of mood disorders, Trends in cognitive sciences 16 (1) (2012) 61–71.

[18] A. S. Widge, D. D. Dougherty, Deep brain stimulation for treatment-refractory mood and obsessive-compulsive disorders, Current Behavioral Neuroscience Reports 2 (4) (2015) 187–197.

[19] U. Braun, A. Schaefer, R. F. Betzel, H. Tost, A. Meyer-Lindenberg, D. S. Bassett, From maps to multi-dimensional network mechanisms of mental disorders, Neuron 97 (1) (2018) 14–31.

[20] J. Kuhn, W. Gaebel, J. Klosterkoetter, C. Woopen, Deep brain stimulation as a new therapeutic approach in therapy-resistant mental disorders: ethical aspects of investigational treatment, European Archives of Psychiatry and Clinical Neuroscience 259 (2) (2009) 135–141.

[21] M. Dandekar, A. Fenoy, A. Carvalho, J. Soares, J. Quevedo, Deep brain stimulation for treatment-resistant depression: an integrative review of preclinical and clinical findings and translational implications, Molecular psychiatry 23 (5) (2018) 1094–1112.

[22] K. W. Scangos, G. S. Makhoul, L. P. Sugrue, E. F. Chang, A. D. Krystal, State-dependent responses to intracranial brain stimulation in a patient with depression, Nature Medicine 27 (2) (2021) 229–231.

[23] C. C. Lee, C. C. Chou, F. J. Hsiao, Y. H. Chen, C. F. Lin, C. J. Chen, S. J. Peng, H. L. Liu, H. Y. Yu, Pilot study of focused ultrasound for drug-resistant epilepsy, Epilepsia 63 (1) (2022) 162–175. doi:10.1111/epi.17105.

[24] N. Li, P. Gaur, K. Quah, K. Butts Pauly, Improving in situ acoustic intensity estimates using MR acoustic radiation force imaging in combination with multifrequency MR elastography, Magnetic Resonance in Medicine 88 (4) (2022) 1673–1689. doi:10.1002/mrm.29309.

[25] J. A. Cain, N. M. Spivak, J. P. Coetzee, J. S. Crone, M. A. Johnson, E. S. Lutkenhoff, C. Real, M. Buitrago-Blanco, P. M. Vespa, C. Schnakers, M. M. Monti, Ultrasonic Deep Brain Neuromodulation

in Acute Disorders of Consciousness: A Proof-of-Concept (2022). doi:10.3390/brainsci12040428.

[26] J. M. Stern, N. M. Spivak, S. A. Becerra, T. P. Kuhn, A. S. Korb, D. Kronemyer, N. Khanlou, S. D. Reyes, M. M. Monti, C. Schnakers, P. Walshaw, I. Keselman, M. S. Cohen, W. Yong, I. Fried, S. E. Jordan, M. E. Schafer, J. Engel, A. Bystritsky, Safety of focused ultrasound neuromodulation in humans with temporal lobe epilepsy, Brain Stimulation 14 (4) (2021) 1022–1031. doi:10.1016/j.brs.2021.06.003.

[27] W. Lee, S. D. Lee, M. Y. Park, J. Yang, S.-S. Yoo, Evaluation of polyvinyl alcohol cryogel as an acoustic coupling medium for low-intensity transcranial focused ultrasound, International Journal of Imaging Systems and Technology 24 (4) (2014) 332–338. doi:10.1002/ima.22110.

[28] T. Riis, M. Wilson, J. Kubanek, Controlled delivery of ultrasound through the head for effective and safe therapies of the brain, bioRxiv (2022.12.16.520788) (2022).

[29] F. Vignon, J. F. Aubry, M. Tanter, A. Margoum, M. Fink, Adaptive focusing for transcranial ultrasound imaging using dual arrays, The Journal of the Acoustical Society of America 120 (5) (2006) 2737–2745. doi:10.1121/1.2354073.

[30] T. Webb, M. Wilson, O. Henrik, J. Kubanek, Remus: System for remote deep brain interventions, BioRxiv (2022).

[31] L. S. Morris, S. Costi, A. Tan, E. R. Stern, D. S. Charney, J. W. Murrough, Ketamine normalizes subgenual cingulate cortex hyper-activity in depression, Neuropsychopharmacology 45 (6) (2020) 975–981.

[32] M. Plaksin, E. Kimmel, S. Shoham, Cell-type-selective effects of intramembrane cavitation as a unifying theoretical framework for ultrasonic neuromodulation, eneuro 3 (3) (2016).

[33] O. Naor, S. Krupa, S. Shoham, Ultrasonic neuromodulation, Journal of Neural Engineering 13 (3) (2016) 031003.

[34] J. Blackmore, S. Shrivastava, J. Sallet, C. R. Butler, R. O. Cleveland, Ultrasound neuromodulation: A review of results, mechanisms and safety, Ultrasound in medicine & biology 45 (7) (2019) 1509–1536.

[35] W. Rief, A. J. Barsky, J. A. Glombiewski, Y. Nestoriuc, H. Glaesmer, E. Braehler, Assessing general side effects in clinical trials: reference data from the general population, Pharmacoepidemiology and drug safety 20 (4) (2011) 405–415.

[36] K. Hynynen, J. Sun, Trans-skull ultrasound therapy: the feasibility of using image-derived skull thickness information to correct the phase distortion, IEEE transactions on ultrasonics, ferroelectrics, and frequency control 46 (3) (1999) 752–755.

[37] L. Marsac, D. Chauvet, R. La Greca, A.-L. Boch, K. Chaumoitre, M. Tanter, J.-F. Aubry, Ex vivo optimisation of a heterogeneous speed of sound model of the human skull for non-invasive transcranial focused ultrasound at 1 mhz, International Journal of Hyperthermia 33 (6) (2017) 635–645.

[38] T. D. Webb, S. A. Leung, J. Rosenberg, P. Ghanouni, J. J. Dahl, N. J. Pelc, K. B. Pauly, Measurements of the relationship between ct hounsfield units and acoustic velocity and how it changes with photon energy and reconstruction method, IEEE transactions on ultrasonics, ferroelectrics, and frequency control 65 (7) (2018) 1111–1124.

[39] S. A. Leung, T. D. Webb, R. R. Bitton, P. Ghanouni, K. B. Pauly, A rapid beam simulation framework for transcranial focused ultrasound, Scientific reports 9 (1) (2019) 1–11.

[40] L. Deng, A. Hughes, K. Hynynen, A noninvasive ultrasound resonance method for detecting skull induced phase shifts may provide a signal for adaptive focusing, IEEE Transactions on Biomedical Engineering 67 (9) (2020) 2628–2637.

[41] H. Johansen-Berg, D. Gutman, T. Behrens, P. Matthews, M. Rushworth, E. Katz, A. Lozano, H. Mayberg, Anatomical connectivity of the subgenual cingulate region targeted with deep brain stimulation for treatment-resistant depression, Cerebral cortex 18 (6) (2008) 1374–1383.

[42] E. Rodríguez-Cano, S. Sarró, G. Monté, T. Maristany, R. Salvador, P. McKenna, E. Pomarol-Clotet, Evidence for structural and functional abnormality in the subgenual anterior cingulate cortex in major depressive disorder, Psychological medicine 44 (15) (2014) 3263–3273.

[43] L. Alexander, H. F. Clarke, A. C. Roberts, A focus on the functions of area 25, Brain sciences 9 (6) (2019) 129.

[44] R. J. Davidson, Anxiety and affective style: role of prefrontal cortex and amygdala, Biological psychiatry 51 (1) (2002) 68–80.

[45] S. J. Bishop, Neurocognitive mechanisms of anxiety: an integrative account, Trends in cognitive sciences 11 (7) (2007) 307–316.

[46] K. M. Tye, R. Prakash, S.-Y. Kim, L. E. Fenno, L. Grosenick, H. Zarabi, K. R. Thompson, V. Gradinaru, C. Ramakrishnan, K. Deisseroth, Amygdala circuitry mediating reversible and bidirectional control of anxiety, Nature 471 (7338) (2011) 358–362.

[47] W. Lee, H.-C. Kim, Y. Jung, Y. A. Chung, I.-U. Song, J.-H. Lee, S.-S. Yoo, Transcranial focused ultrasound stimulation of human primary visual cortex, Scientific Reports 6 (2016).

[48] L. Ai, J. K. Mueller, A. Grant, Y. Eryaman, W. Legon, Transcranial focused ultrasound for BOLD fMRI signal modulation in humans, Proceedings of the Annual International Conference of the IEEE Engineering in Medicine and Biology Society, EMBS 2016-Octob (2016) 1758–1761. arXiv:1603.00415, doi:10.1109/EMBC.2016.7591057.

[49] L. Ai, P. Bansal, J. K. Mueller, W. Legon, Effects of transcranial focused ultrasound on human primary motor cortex using 7T fMRI: a pilot study, BMC neuroscience 19 (1) (2018) 1–10.

[50] S. T. Brinker, F. Preiswerk, P. J. White, T. Y. Mariano, N. J. McDannold, E. J. Bubrick, Focused Ultrasound Platform for Investigating Therapeutic Neuromodulation Across the Human Hippocampus, Ultrasound in Medicine and Biology 46 (5) (2020) 1270–1274. doi:10.1016/j.ultrasmedbio.2020.01.007.

[51] W. Lee, H. Kim, Y. Jung, I. U. Song, Y. A. Chung, S. S. Yoo, Image-guided transcranial focused ultrasound stimulates human primary somatosensory cortex, Scientific Reports 5 (2015) 1–10. doi:10.1038/srep08743.

[52] L. Verhagen, C. Gallea, D. Folloni, C. Constans, D. E. Jensen, H. Ahnine, L. Roumazeilles, M. Santin, B. Ahmed, S. Lehéricy, et al., Offline impact of transcranial focused ultrasound on cortical activation in primates, Elife 8 (2019) e40541.

[53] D. Folloni, L. Verhagen, R. B. Mars, E. Fouragnan, C. Constans, J.-F. Aubry, M. F. Rushworth, J. Sallet, Manipulation of subcortical and deep cortical activity in the primate brain using transcranial focused ultrasound stimulation, Neuron 101 (6) (2019) 1109–1116.

[54] N. Khalighinejad, A. Bongioanni, L. Verhagen, D. Folloni, D. Attali, J.-F. Aubry, J. Sallet, M. F. Rushworth, A basal forebrain-cingulate circuit in macaques decides it is time to act, Neuron 105 (2) (2020) 370–384.

[55] J. L. Sanguinetti, S. Hameroff, E. E. Smith, T. Sato, C. M. Daft, W. J. Tyler, J. J. Allen, Transcranial focused ultrasound to the right prefrontal cortex improves mood and alters functional connectivity in humans, Frontiers in Human Neuroscience 14 (2020). doi:10.3389/fnhum.2020.00052.

[56] S. J. Reznik, J. L. Sanguinetti, W. J. Tyler, C. Daft, J. J. Allen, A double-blind pilot study of transcranial ultrasound (tus) as a five-day intervention: Tus mitigates worry among depressed participants, Neurology Psychiatry and Brain Research 37 (2020). doi:10.1016/j.npbr.2020.06.004.

[57] P. Pouget, S. Frey, H. Ahnine, D. Attali, J. Claron, C. Constans, J. F. Aubry, F. Arcizet, Neuronavigated repetitive transcranial ultrasound stimulation induces long-lasting and reversible effects on oculomotor performance in non-human primates, Frontiers in Physiology 11 (8 2020). doi:10.3389/fphys.2020.01042.

[58] F. Munoz, A. Meaney, A. Gross, K. Liu, A. N. Pouliopoulos, D. Liu, E. E. Konofagou, V. P. Ferrera, Long term study of motivational and cognitive effects of low-intensity focused ultrasound neuromodulation in the dorsal striatum of nonhuman primates, Brain Stimulation 15 (2022). doi:10.1016/j.brs.2022.01.014.

[59] B. C. Gibson, J. L. Sanguinetti, B. W. Badran, A. B. Yu, E. P. Klein, C. C. Abbott, J. T. Hansberger, V. P. Clark, Increased excitability induced in the primary motor cortex by transcranial ultrasound stimulation, Frontiers in Neurology 9 (NOV) (2018) 1–10. doi:10.3389/fneur.2018.01007.

[60] B. Clennell, T. G. Steward, M. Elley, E. Shin, M. Weston, B. W. Drinkwater, D. J. Whitcomb, Transient ultrasound stimulation has lasting effects on neuronal excitability, Brain Stimulation 14 (2) (2021) 217–225.

[61] J. L. Sanguinetti, S. Hameroff, E. E. Smith, T. Sato, C. M. Daft, W. J. Tyler, J. J. Allen, Transcranial focused ultrasound to the right prefrontal cortex improves mood and alters functional connectivity in humans, Frontiers in Human Neuroscience 14 (2020) 52.

SUPPLEMENTARY MATERIAL:

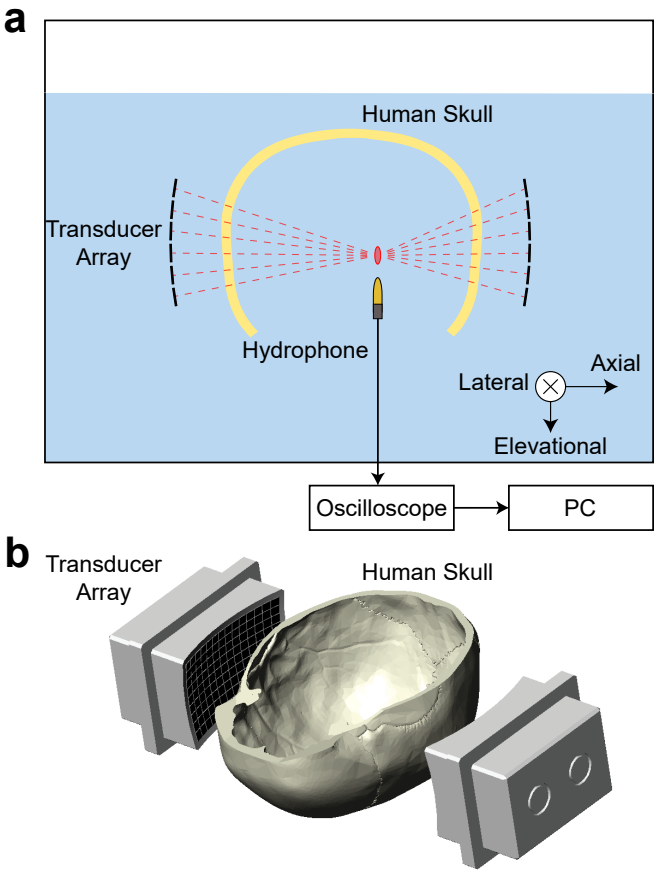

Fig. 1: **Experimental setup of hydrophone field scan through ex-vivo skull.**
a, Pressure field measurements are made through intact ex-vivo skull calvaria using a hydrophone and a three-dimensional positioner. **b,** Rendering of transducer array positioning relative to skull calveria.

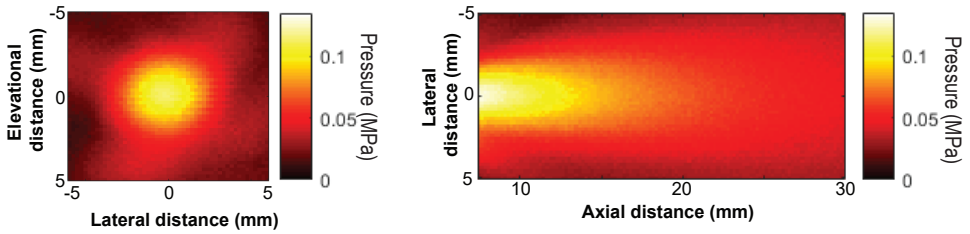

Fig. 2: **Pressure field produced by each individual element.**
Pressure field of single element of the transducer phased arrays measured with hydrophone field scan. Elevational-Lateral plane was taken at an axial distance of 7.5 mm from the transducer face.

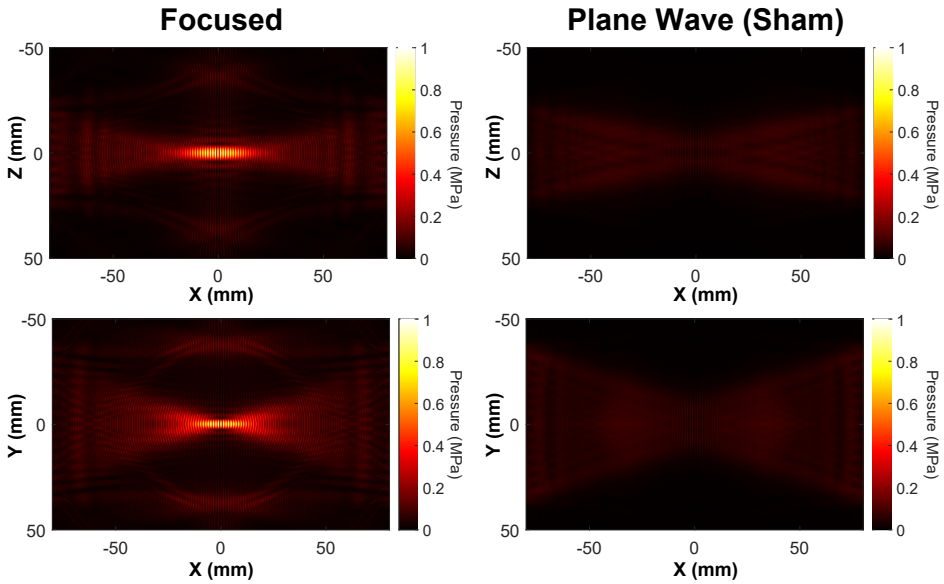

Fig. 3: **Pressure field of focused vs unfocused plane wave (sham) stimulation.**
Pressure field of the phased arrays when focusing at target (left) and when emitting an unfocused plane wave (right) as in our sham stimulation. The spatial peak pressure of the focused field is 1 MPa (31.1 W/cm^2) while the spatial peak pressure field of the plane wave is 0.098 MPa (0.30 W/cm^2).

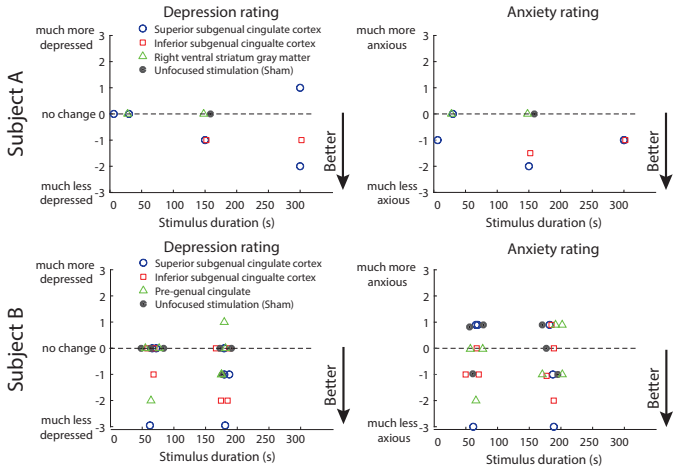

Fig. 4: **Mood scores for each modulated target and each stimulus duration.**
Same format as in **Fig. 4**, for each target and stimulus duration.